Research Article | Open Access

Microstructures

Liu *et al*. *Microstructures* **2026**, *6*, 20260123 **DOI:**10.20517/microstructures.2026.57

Direct Z-scheme siloxene germanane nanosheet heterojunctions for broadband photodetection and ultrasensitive photoelectrochemical sensing

Runqi Liu[1,2,3,#], Huiyu Chen[1,2,3,#], Weikang Yuan[1,2,3], Hui Fu[1,2,3], Fulai Zhao[1,2,3,4], Yiyu Feng[1,2,3]

Keywords:
Silicene, germanene, direct bandgap semiconductor, 2D Z-scheme heterojunction, PEC photodetector, PEC sensor

Citation: Liu, R.; Chen, H.; Yuan, W.; Fu, H.; Zhao, F.; Feng, Y. Direct Z-scheme siloxene germanane nanosheet heterojunctions for broadband photodetection and ultrasensitive photoelectrochemical sensing. *Microstructures* **2026**, *6*, 20260123. https://dx.doi.org/10.20517/microstructures.2026.57

Received: 31 Mar 2026 **First Decision:** 29 May 2026 **Revised:** 27 Aug 2026 **Accepted:** 28 Aug 2026 **Published:** 18 Sep 2026

Academic Editor: Chunqiang Zhuang
Copy Editor: Fangling Lan
Production Editor: Fangling Lan

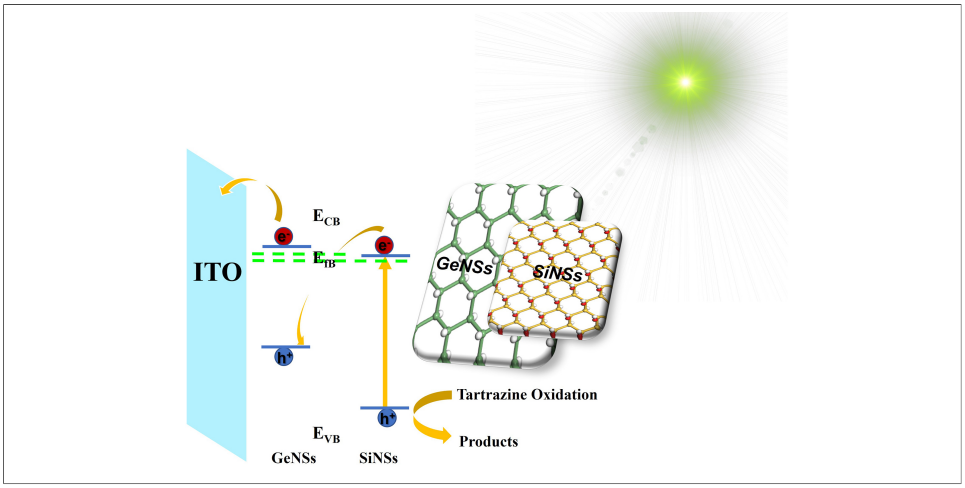

Abstract

Siloxene and germanane are two-dimensional (2D) direct-bandgap semiconductors that hold promise for a range of applications, including photocatalysis, electronics, and photodetectors (PDs). In this study, we explore a novel direct Z-scheme 2D-2D siloxene/germanane heterojunction fabricated via wet-mixing self-assembly. This heterojunction exhibits superior light absorption compared with the individual nanosheets. Notably, when employed as a photoelectrode material for photoelectrochemical (PEC) PDs, it shows a marked photoresponse across the 365-980 nm range, with a peak responsivity at 520 nm. Specifically, under 520 nm illumination, its responsivity surpasses those of siloxene and germanane nanosheets by factors of 221.3 and 3.7, respectively. Remarkably, even at zero bias, it achieves a high photoresponsivity of 3.75 μA W^{-1} and a detectivity of 1.3 × 10^8 Jones, demonstrating excellent self-powered performance. Owing to its exceptional light sensitivity at 520 nm, the Z-scheme heterojunction is particularly well

[1]Discipline and Technology Center for High Temperature Functional Ceramics, Shandong University of Technology, Zibo 255000, Shandong, China.
[2]Shandong Key Laboratory of Functional-Structural Integrated Ceramics, Shandong University of Technology, Zibo 255000, Shandong, China.
[3]School of Materials Science and Engineering, Shandong University of Technology, Zibo 255000, Shandong, China.
[4]Shandong Chambroad Holding Group Co., Ltd., Binzhou 256500, Shandong, China.
[#]Authors contributed equally.

Correspondence to: Prof. Fulai Zhao, Discipline and Technology Center for High Temperature Functional Ceramics, Shandong University of Technology, Zibo 255000, Shandong, China; Shandong Key Laboratory of Functional-Structural Integrated Ceramics, Shandong University of Technology, Zibo 255000, Shandong, China; School of Materials Science and Engineering, Shandong University of

Technology, Zibo 255000, Shandong, China; Shandong Chambroad Holding Group Co., Ltd., Binzhou 256500, Shandong, China. E-mail: jayfly@sdut.edu.cn

suited for the PEC photodetection of tartrazine, offering an ultralow detection limit of 0.3 pM and a broad linear range from 1 pM to 1 μM in aqueous media. Overall, this research highlights the considerable potential of the siloxene/germanane heterojunction for advanced optoelectronic applications, including high-performance PDs and PEC sensors.

INTRODUCTION

In recent years, two-dimensional materials (2D) have attracted widespread attention due to their unique properties and broad application prospects. 2D materials such as MXene, phosphorene, silicene, germanene and transition metal dichalcogenides have been extensively used in optoelectronic devices, solar cells, photoelectrochemical (PEC) sensors, and gas sensors[1-5]. They possess a large specific surface area, high electron mobility, abundant active sites, and efficient carrier separation capabilities. Among these materials, siloxene and germanane are particularly noteworthy for their excellent electronic and optoelectronic properties[6]. They are derivatives of 2D silicene and germanene, both of which have a honeycomb-like 2D structure similar to that of graphene. The difference is that the atoms in the honeycomb skeleton are not coplanar, but adopt a buckled structure. Siloxene is composed of silicon, oxygen, and hydrogen atoms, with hydrogen atoms and hydroxyl groups covalently bonded to the upper and lower surfaces of the honeycomb-like silicene[7]; germanane is composed of germanium and hydrogen atoms, with hydrogen atoms covalently bonded to the upper and lower surfaces of the honeycomb-like germanene framework[8]. Both siloxene and germanane exhibit direct bandgap semiconducting properties and good visible-light absorption[9]. They also possess abundant surface-active sites, high theoretical carrier mobility, and tunable bandgap structures, rendering them suitable for transistors[10,11], photodetectors (PDs)[12,13], metal-ion batteries[14-16], capacitors[17,18], electrochemical sensors[19-23], as well as various photocatalytic and photoelectrocatalytic applications[23-29].

However, the photoelectric performance of siloxene and germanane when used individually may be limited by the recombination of photogenerated electrons and holes. Siloxene's wide bandgap (approximately 2.5 eV) restricts its absorption to ultraviolet and a limited range of visible wavelengths, while germanane's narrower bandgap (about 1.59 eV) allows it to effectively absorb ultraviolet, visible, and near-infrared light[9]. Modulating the properties of these 2D materials can enhance their performance and improve their adaptability for diverse applications[30-32]. Constructing heterojunctions is an effective strategy for improving photoelectric transport properties and enhancing device performance[33-35].

Recently, Z-scheme heterojunctions have attracted considerable attention due to their ability to simultaneously achieve efficient charge separation and strong redox capability[36-38]. In a Z-scheme system, the photogenerated electrons in the conduction band of one semiconductor recombine with the holes in the valence band of the other, leaving the electrons with stronger reducing power and the holes with stronger oxidizing power at their respective sides[39,40]. This charge transfer pathway not only suppresses carrier recombination but also preserves the maximum redox potentials for both reduction and oxidation reactions. Various Z-scheme heterojunctions based on 2D materials, such as g-C_3N_4/MXene[41], TiO_2/MoS_2[42], and WO_3/g-C_3N_4[43], have been reported for photocatalytic and PEC applications. However, to the best of our knowledge, there have been no reports on the electronic and optical properties of siloxene/germanane heterojunctions and their applications in optoelectronic devices.

PEC PDs and sensors are key components of advanced sensing technologies[44,45]. PDs convert light signals into electrical signals, whereas PEC sensors employ light to drive electrochemical reactions, enabling the detection of specific analytes. Both technologies are essential for the development of sensitive and efficient

detection methods in areas such as food safety and environmental monitoring[46-50]. The presence of food additives poses a significant public health concern. Traditional detection methods, such as ultraviolet-visible (UV-vis) spectroscopy, fluorescence emission spectroscopy, high-performance liquid chromatography, and gas chromatography, often suffer from drawbacks such as long reaction times, costly equipment, high detection costs, and complex procedures[51]. Therefore, there is an urgent need for convenient, accurate, and low-cost food safety detection methods. PEC sensors employ light as the excitation source and photocurrent as the detection signal, offering rapid response, high sensitivity, low cost, and flexibility, and thus exhibiting great promise for various applications[52,53]. As a key component of PEC sensors, the performance of photosensitive materials plays a decisive role in determining the sensitivity, selectivity, and stability of the sensor.

In this study, we prepared germanane nanosheets (GeNSs) and siloxene nanosheets (SiNSs) via liquid-phase exfoliation using polyvinylpyrrolidone (PVP) as a surfactant, and subsequently assembled them into GeNSs/SiNSs nanocomposites through liquid-phase assembly. The structural, electronic, and optoelectronic properties of the resulting heterojunctions were systematically investigated through a combination of theoretical calculations, materials characterization, and PEC measurements. Particular attention was paid to the heterojunction formation mechanism, charge transfer dynamics, and the resulting photoresponse performance. Furthermore, we explored the potential application of the GeNSs/SiNSs heterojunction as a PEC photosensitive material for the detection of food additives, specifically tartrazine, as a model analyte. This work aims to demonstrate the feasibility of constructing high-performance, self-powered PEC PDs and ultrasensitive sensors based on 2D/2D germanane/siloxene heterojunctions.

EXPERIMENTAL

Preparation of layered 2D/2D GeNSs/SiNSs nanocomposites

GeNSs/SiNSs nanocomposites were prepared via wet-mixing self-assembly of few-layer GeNSs and SiNSs. The resulting nanocomposites were designated H1, H2, and H3 for mass ratios of GeNSs to SiNSs of 1:9, 3:7, and 1:1, respectively. The few-layer GeNSs and SiNSs were obtained through ultrasonic exfoliation assisted by PVP solution. Germanane and siloxene were synthesized following the literature[8,27]. Detailed procedures are provided in the Supplementary Materials.

Photoelectrochemical measurements

Photoelectrochemical measurements were performed at room temperature using an electrochemical workstation equipped with a three-electrode cell. Illumination was provided by a 300 W xenon lamp and monochromatic light at 365, 405, 520, 635, 750, 808, and 980 nm to irradiate the working electrode, and the corresponding light intensities were designated as Level I, II, III, and IV [Supplementary Table 1]. Detailed procedures are described in the Supplementary Materials.

PEC detection of tartrazine

A three-electrode system consisted of an Indium tin oxide (ITO)/GeNSs-SiNSs heterostructure electrode as the working electrode, a Pt plate as the counter electrode and a saturated calomel electrode (SCE) as the reference electrode. Under 520 nm light irradiation (Level III according to Supplementary Table 1), the blank photocurrent (blank control group) of the ITO/GeNSs-SiNSs heterostructure electrode was measured in 40 mL of 0.1 M Na_2SO_4 under a bias potential of 0.3 V. Then, the electrode was immersed in tartrazine solution (with 0.1 M Na_2SO_4 as the supporting electrolyte) for 10 min prior to measurement. The photocurrent measurements were performed under the same applied bias and illumination conditions as those for the blank control group. The photocurrent was recorded under pulsed light (20 s on/20 s off), and the light power density was set to Level III according to Supplementary Table 1. After the measurement, the electrode was taken out, rinsed with deionized water, and dried under nitrogen. The test conditions were

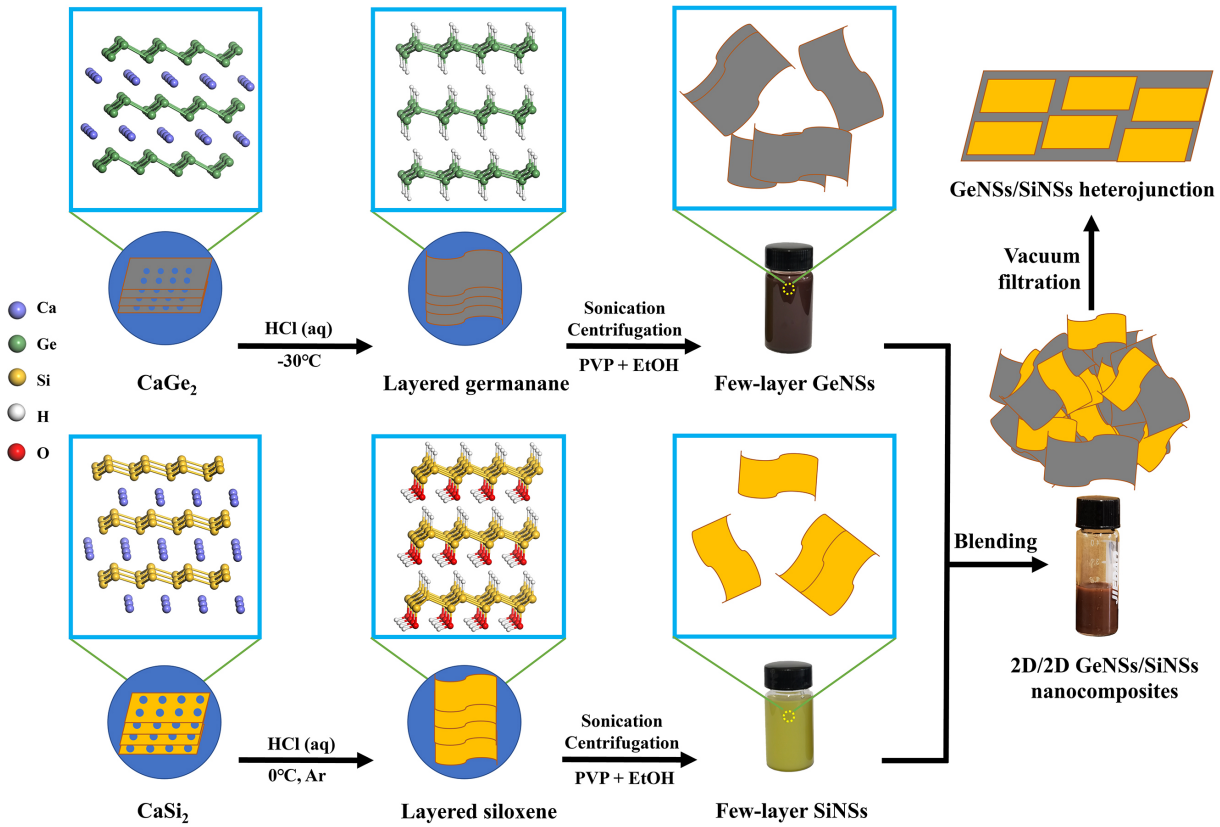

Figure 1. Schematic diagram of preparation process of 2D/2D GeNSs/SiNSs nanocomposites.

kept unchanged, and the photocurrent response for the next different tartrazine concentration was subsequently measured to obtain the correlation between photocurrent and tartrazine concentration. In addition, stability measurements were conducted in 10^{-11} M tartrazine solution under 520 nm light (Level III). A bias potential of 0.3 V was applied, and pulsed-light mode (5 s on/5 s off) was adopted for the test. All the PEC experiments were performed at room temperature.

RESULTS AND DISCUSSION

2D/2D GeNSs/SiNSs nanocomposites were prepared by a facile ultrasonication-centrifugation process and a liquid-phase assembly technique, as shown in Figure 1. The results of atomic force microscopy (AFM) characterization show that the thickness of GeNSs ranges from 3.5 to 4 nm [Supplementary Figure 1A], while the thickness of SiNSs ranges from 1.5 to 2 nm [Supplementary Figure 1B], indicating that the exfoliated nanosheets are few-layer nanosheets; notably, the size of GeNSs is apparently larger than that of SiNSs. The Fourier transform infrared (FTIR) spectra [Supplementary Figure 1C] indicate that GeNSs/SiNSs nanocomposites exhibit clear main characteristic peaks of pure germanane and siloxene. Raman spectra [Supplementary Figure 1D] also indicate that all characteristic Raman peaks of both germanane and siloxene can be observed in GeNSs/SiNSs nanocomposite samples.

Supplementary Figure 1E shows the crystal structure of GeNSs/SiNSs nanocomposites. Due to the amorphous nature of siloxene[17,18,25,54], no obvious diffraction peaks of siloxene were observed in the GeNSs/SiNSs composite, while the characteristic diffraction peaks of germanane are clearly displayed in the GeNSs/SiNSs composite. However, the difference is that the peak position at around 15° representing the interlayer spacing of germanane varies slightly. This is because SiNSs and GeNSs are stacked together,

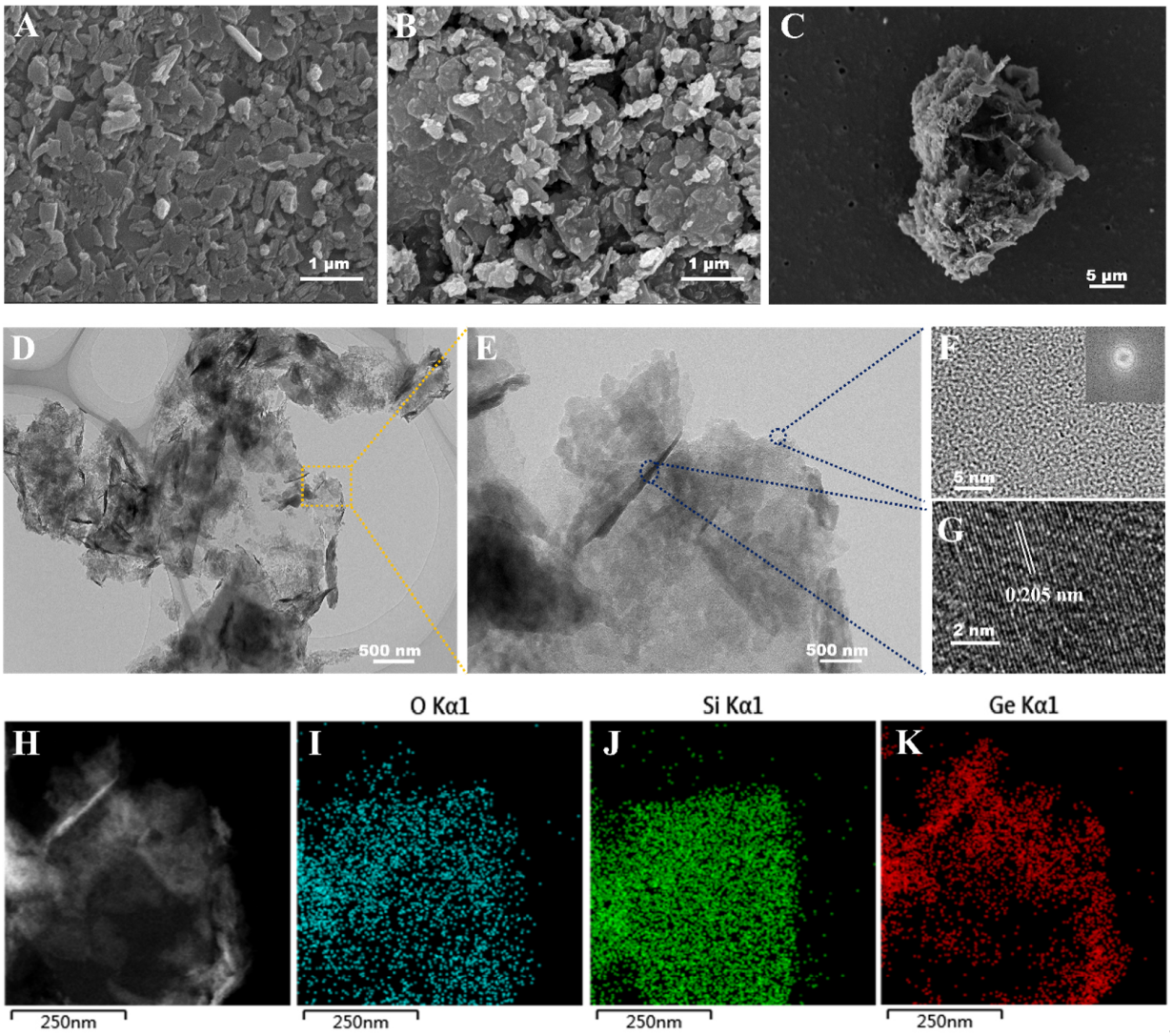

Figure 2. (A-C) SEM images of (A) SiNSs, (B) GeNSs and (C) H2 nanocomposites; (D) TEM image of H2 nanocomposites, (E) HRTEM of H2 nanocomposites; (F) HRTEM image of the dark blue circle in (E), inset is the corresponding fast Fourier transform (FFT) pattern; (G) HRTEM image of the yellow circle in (E), inset is the corresponding fast Fourier transform (FFT) pattern. (H-K) STEM image of the GeNSs/SiNSs composites (H) with its corresponding EDS elemental mapping of (I) O, (J) Si, and (K) Ge elements.

resulting in a change in the interlayer spacing of the composites. The X-ray diffraction, FTIR, and Raman results demonstrate that in GeNSs/SiNSs composites, GeNSs and SiNSs are physically stacked together via van der Waals interactions.

Figure 2A and B show scanning electron microscope (SEM) images of SiNSs and GeNSs obtained by exfoliation. The average size of SiNSs is about 365 nm, while that of GeNSs is about 574 nm, and the size distribution of SiNSs is relatively more uniform, whereas the overall size of GeNSs is larger than that of SiNSs. After the assembly of GeNSs and SiNSs, a three-dimensional stacked structure is formed, as shown in Figure 2C. Because the transmission electron microscope (TEM) morphology of GeNSs and SiNSs is very similar, it is difficult to clearly distinguish them based solely on morphology [Figure 2D]. Through the high-resolution TEM (HRTEM) characterization of the nanosheets in the dark blue dotted circles [Figure 2E], clear lattice fringes and amorphous structures can be observed, respectively.

The lattice fringes are characteristic of GeNSs, and the amorphous regions are characteristic of SiNSs, which is consistent with the fast Fourier transform (FFT) patterns (insets in Figure 2F and G). Scanning transmission electron microscope (STEM) [Figure 2H] and TEM elemental mapping images [Figure 2I-K] show that Si and Ge are evenly distributed, and their distributions mostly overlap, with Ge covering almost all areas of the composite material. Combined with the characterization results of HRTEM and FFT, it is shown that the relatively small SiNSs are covered or wrapped by the larger GeNSs, forming a tightly stacked assembly. As is well known, the formation of heterojunctions helps to improve the transport efficiency and separation of charge carriers[34,55,56].

To investigate the surface composition and chemical state of the heterostructure, we conducted X-ray photoelectron spectroscopy (XPS) characterization, as shown in Figure 3. The XPS survey spectra for the heterostructure shown in Figure 3A confirmed the presence of Ge, Si, and O, consistent with the results obtained from energy dispersive spectrometry (EDS) mapping. The high-resolution Ge 3d XPS spectrum of GeNSs in Figure 3B revealed four peaks at 28.39, 28.91, 29.54, and 30.76 eV. The peak at 28.39 eV corresponds to Ge-Ge bonds in elemental Ge[57]. The peaks at 28.91 and 29.54 eV are attributed to the Ge 3d5/2 and Ge 3d3/2 components of GeNSs[58], respectively. The weaker peak at 30.76 eV is likely due to Ge-O bonds resulting from the surface oxidation of GeNSs[14]. For SiNSs, the Si 2p XPS spectrum in Figure 3C was deconvoluted into two peaks at 99.9 and 103.2 eV, representing Si-Si and Si-O bonds, respectively. Notable shifts in the binding energies of the Ge 3d and Si 2p peaks were observed for the heterostructure, as shown in Figure 3B and C. All Si 2p peaks in the heterostructure shifted markedly to lower binding energies compared with those of SiNSs, while the Ge 3d peaks shifted to higher values than those in GeNSs. This shift indicates electron transfer from GeNSs to SiNSs, evidencing a strong interaction between the two components within the heterostructure. This interaction may facilitate the separation and transfer of electron-hole pairs[55,59,60].

The O 1s XPS spectra of the GeNSs/SiNSs heterostructure [Figure 3D] were fitted to four peaks at 530.8, 531.6, 532.2, and 533.0 eV. The peaks at 532.2 and 533.0 eV are assigned to Si-O bonds and the surface oxygen from hydroxyl groups, respectively, originating from SiNSs. The peak at 530.8 eV corresponds to Ge-O bonds from GeNSs. Importantly, the peak at 531.6 eV, originating from both GeNSs (531.5 eV) and SiNSs (531.76 eV), corresponds to adsorbed oxygen species, indicating the presence of oxygen vacancies in both materials, as confirmed by our previous work[27]. These oxygen vacancies could enhance the separation of photoexcited charge carriers and extend the light response into the visible and near-infrared regions (NIR), thus improving photoreactivity[61,62]. Additionally, we observed positive shifts in the O 1s binding energies for GeNSs and negative shifts for SiNSs within the heterostructure, consistent with the shifts in the binding energies of Ge 3d and Si 2p. This further corroborates the formation of the GeNSs/SiNSs heterostructure with strong interaction between the two components[35].

Figure 3E presents the UV-vis-NIR spectra of pure GeNSs, SiNSs, and GeNSs/SiNSs heterojunctions H1, H2, and H3. SiNSs exhibit an absorption onset at around 476 nm, whereas GeNSs show broad light absorption across the UV, visible, and even NIR regions, with enhanced absorption between 400 and 700 nm. The incorporation of GeNSs into SiNSs extends the absorption range from nearly 500 nm to over 800 nm, with enhanced absorption intensity in the visible region, attributed to the synergistic effect between SiNSs and GeNSs[63,64]. The increase in photoexcited charge carriers was further demonstrated by subsequent photocurrent measurements. Figure 3F displays the classical Tauc plots, revealing band gaps of 2.60 eV for SiNSs and 1.66 eV for GeNSs, which are in close agreement with reported values[12,25,65].

To assess the photoresponse performance, SiNSs, GeNSs, and heterojunctions H1, H2, and H3 were fabricated into photoelectrodes, and their PEC properties were evaluated in a three-electrode system with 0.5 M Na_2SO_4 as the electrolyte. The transient photocurrent responses were measured under full-spectrum

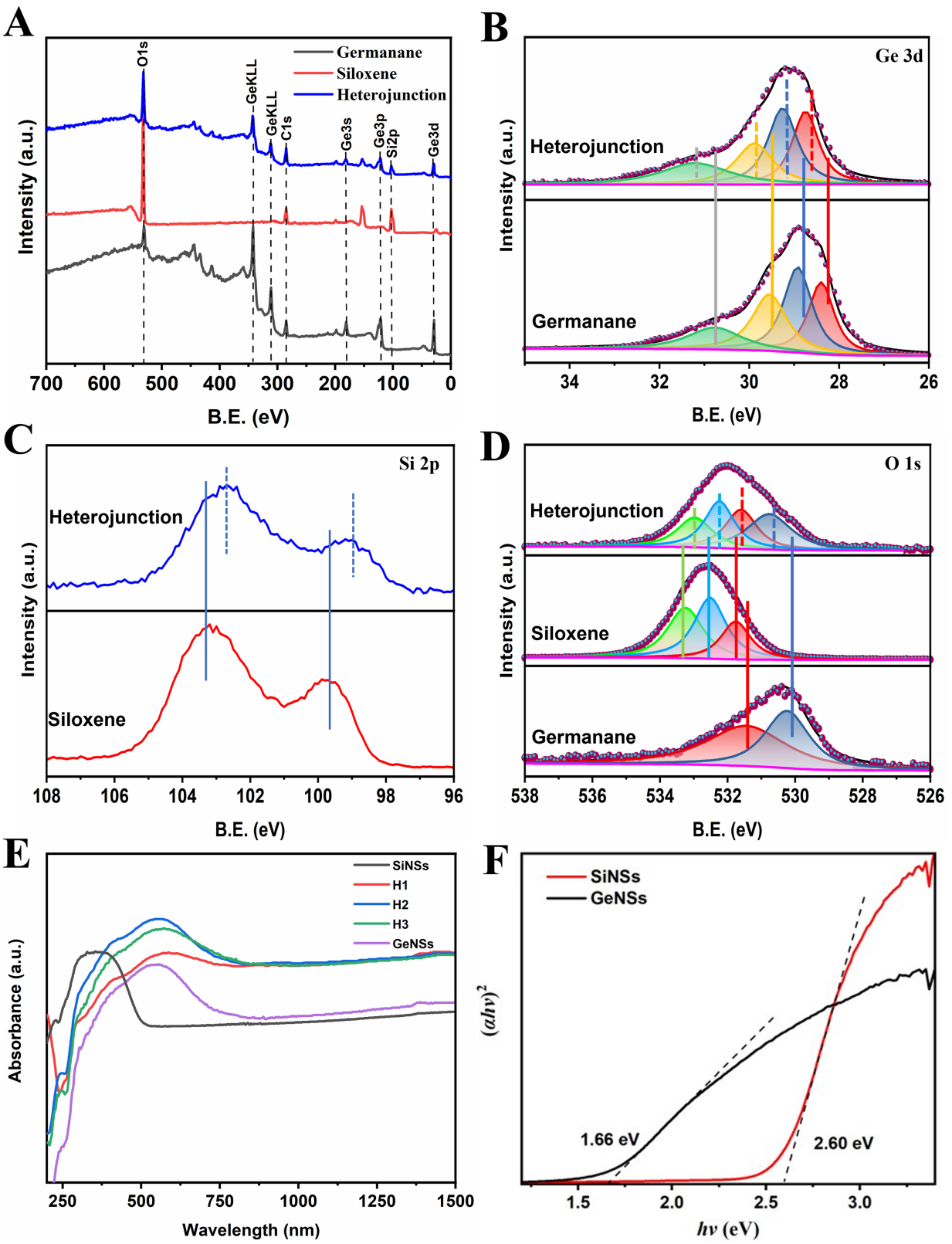

Figure 3. XPS spectra of germanane, siloxene and GeNSs/SiNSs heterostructure. (A) Survey spectra, (B) Ge 3d, (C) Si 2p and (D) O 1s. (E) UV-vis-NIR absorption spectra of GeNSs, SiNSs, and GeNSs/SiNSs H1, H2, and H3. (F) Tauc plot diagram of GeNSs and SiNSs.

illumination from a 300 W xenon lamp at an applied voltage of 0.6 V. As illustrated in Figure 4A, the photocurrent densities of SiNSs and GeNSs were 0.23 and 1.6 μA cm^{-2}, respectively. When GeNSs were introduced into SiNSs to form a composite material, photocurrent densities for mass ratios of 1:9, 3:7, and

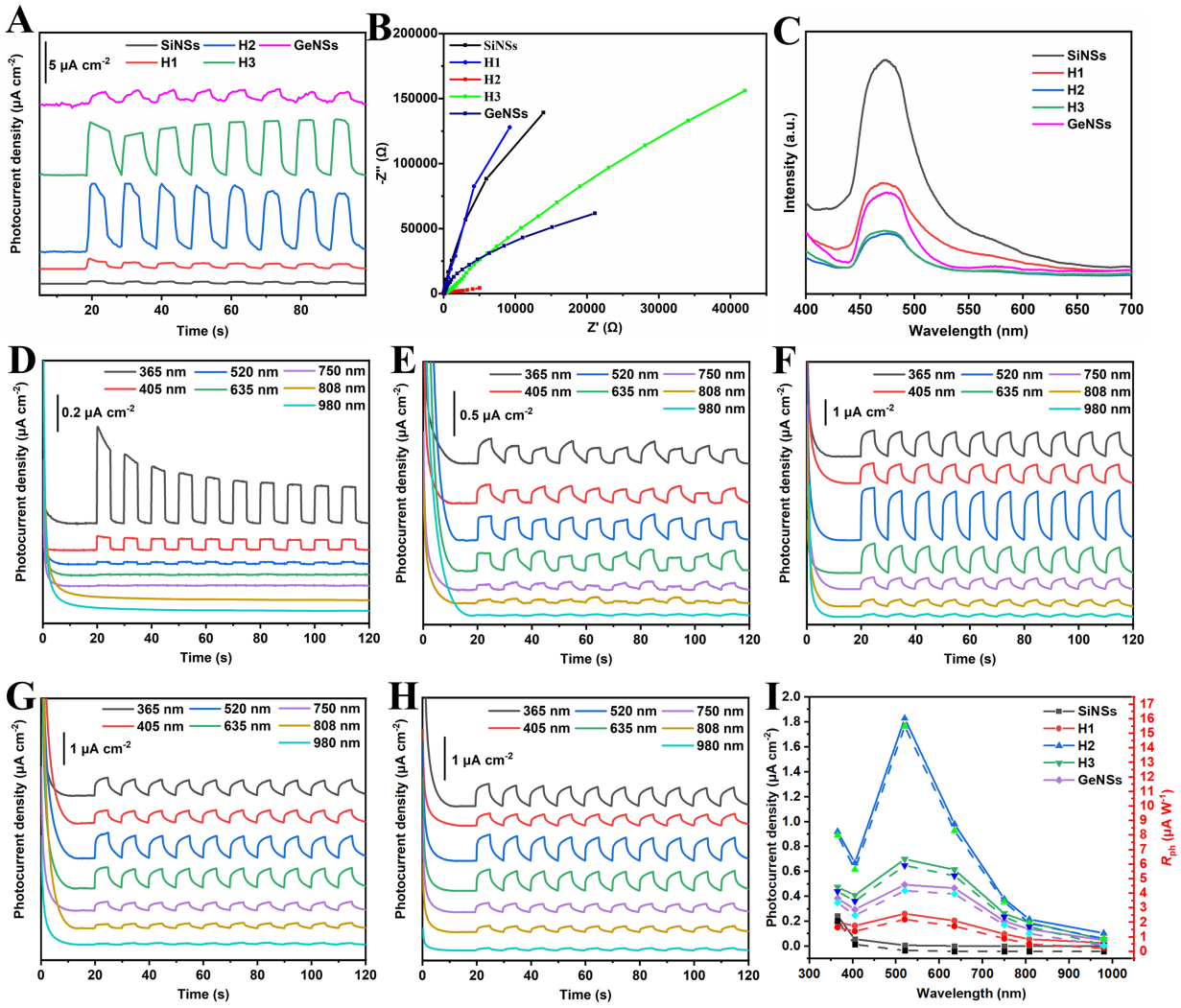

Figure 4. (A) Photoresponse behavior of SiNSs, GeNSs, and nanocomposites of H1, H2, and H3 under a 300 W xenon lamp irradiation at a bias voltage of 0.6 V; (B) Electrochemical impedance spectra (EIS) of SiNSs, GeNSs, H1, H2, and H3; (C) photoluminescence (PL) spectra of SiNSs, GeNSs, H1, H2, and H3. (D-I) Wavelength-dependent photoresponse of (D) SiNSs, (E) H1, (F) H2, (G) H3, and (H) GeNSs at Level III at a bias voltage of 0.6 V. (I) Photocurrent densities and photoresponsivities of SiNSs, H1, H2, H3, and GeNSs-PDs under various monochromatic light wavelengths at Level III under a bias potential of 0.6 V.

1:1 were 0.6, 7.72, and 6.64 μA cm^{-2}, respectively. This indicates that the photocurrent density (P_{ph}) increases with the proportion of GeNSs, reaching a maximum at the 3:7 ratio, and then decreases. This is attributed to the enhanced transport efficiency of photogenerated charge carriers due to the formation of the heterojunction. The optimal ratio of 3:7 yielded the maximum P_{ph}, substantially exceeding those of the individual SiNSs and GeNSs. This is because when the GeNSs content is low, the number of photoactive sites is insufficient. When the ratio reaches 3:7, the distribution of GeNSs on SiNSs achieves an optimal balance, which favors light absorption, exciton dissociation, and charge carrier transport. Further increasing the GeNSs content may lead to agglomeration and an increase in recombination centers, thereby reducing the photocurrent. Electrochemical impedance spectroscopy (EIS) results [Figure 4B] showed that the H2 composite exhibited the smallest semicircle diameter, confirming accelerated electron transfer in the GeNSs/SiNSs heterojunction and indicating a well-formed interface between the two materials.

Photoluminescence (PL) spectra were employed to investigate the recombination and separation behaviors of photogenerated charge carriers. As depicted in Figure 4C, SiNSs exhibited strong emission arising from high recombination rates of photoexcited charge carriers. The introduction of GeNSs resulted in evident PL

quenching in the GeNSs/SiNSs heterojunctions, with H2 showing the lowest PL intensity, indicating the most effective separation of electron-hole pairs and suppressed recombination due to efficient heterostructure formation.

To further investigate the photoresponse characteristics of the heterostructure nanocomposites, we used seven monochromatic light sources with wavelengths ranging from 365 to 980 nm to assess the PEC responses of SiNSs, GeNSs, and the three nanocomposites. The four different power densities for each light source are listed in Supplementary Table 1. The photoresponse of the various electrodes was first compared at a 0.6 V bias under Level III conditions. Figure 4D-I shows that SiNSs displayed apparently lower photocurrent densities compared to GeNSs and the three composites due to strong carrier recombination [Figure 4I]. At 365 nm, SiNSs exhibited a peak P_{ph} and photoresponsivity (R_{ph}) of 0.24 μA cm^{-2} and 2.12 μA W^{-1}, respectively, with values diminishing as the wavelength increased, and no photocurrent was detected above 750 nm [Figure 4D]. This finding is consistent with the wide band gap and limited light absorption of SiNSs. Conversely, GeNSs and all composites demonstrated a broad photoresponse from 365 to 980 nm. Notably, GeNSs and the composites achieved their highest photocurrent densities and responsivities under illumination at 520 nm, in agreement with their UV-vis spectra, which show the strongest absorption peak between 500-600 nm.

Through comparison, we found that the P_{ph} and R_{ph} of the composite H1 (i.e., the mass ratio of GeNSs to SiNSs is 1:9) at different wavelengths are generally higher than those of SiNSs but lower than those of GeNSs. The P_{ph} of H2 (mass ratio of 3:7) and H3 (mass ratio of 1:1) are pronouncedly higher than those of GeNSs and SiNSs, initially increasing and then decreasing with increasing GeNSs content in the composite. This behavior may be attributed to the insufficient heterojunction interface at low GeNSs proportions, resulting in limited improvement in photoelectric performance. As the GeNSs content increases, the enlarged heterogeneous contact interface between GeNSs and SiNSs facilitates the formation of a well-developed heterostructure, leading to a substantial increase in P_{ph}. Under 520 nm illumination, the H2 composite exhibits the highest P_{ph} and R_{ph} among all samples, reaching 1.83 μA cm^{-2} and 15.49 μA W^{-1}, respectively. These values are approximately 221.3 times and 3.7 times higher than those of pristine SiNSs (R_{ph} = 0.07 μA·W^{-1}) and GeNSs (R_{ph} = 4.18 μA·W^{-1}), respectively. This evident enhancement indicates that the H2 composite forms an effective van der Waals heterojunction through intimate interfacial contact between GeNSs and SiNSs.

The enhancement of the broad spectral response over the 365-980 nm range of the composite material by the heterostructure is consistent with the results of subsequent theoretical calculations. In addition, the detectivity of GeNSs at the maximum P_{ph} wavelength of 520 nm (Level III) is 4.4 × 10^7 Jones, whereas that of the H2 composite at this wavelength reaches 1.25 × 10^8 Jones, and that of SiNSs at 520 nm is 3.16 × 10^6 Jones. Even at 365 nm (Level III), whereas SiNSs exhibit their highest P_{ph}, its detectivity is only 8.65 × 10^7 Jones. This indicates that the formation of heterojunction not only enhances the P_{ph} but also reduces the dark current. Notably, at 0 V, the responsivities of H2 at 365, 405, 520, 635, 750, 808, and 980 nm (Level III) are 1.69, 1.21, 3.75, 2.34, 0.92, 0.38, and 0.05 μA W^{-1}, respectively, and the detectivities are 7.0 × 10^7, 4.95 × 10^7, 1.3 × 10^8, 9.1 × 10^7, 3.7 × 10^7, 1.6 × 10^7, 2.1 × 10^6 Jones, respectively, demonstrating excellent self-powered broadband light detection performance (Supplementary Figure 2, under 0 V conditions, the potential difference between the working and counter electrodes arises spontaneously from electrode reactions rather than from an external power source). These performance values surpass those of reported 2D materials and heterojunctions, including GeH[12], BP[66], WS_2[67], 2D Te nanosheets[68], 2D Bi[69], 2D Se[70], 2D InSe nanosheets[71], SnS_2/graphene[72], and WS_2-TiO_2[73], as shown in Supplementary Table 2.

Under 520 nm illumination, the photoresponse test results of the H2-based PD (H2-PD) under different bias voltages [Supplementary Figure 3] show that P_{ph} increases with increasing bias voltage, indicating that a higher bias potential can further improve the photoresponse performance of H2-PD. This is because applying a bias voltage to the working electrode induces potential differences within the material, which promote the separation of photogenerated holes and electrons and increase the carrier concentration, resulting in a marked rise in P_{ph} with bias voltage.

The intensity of incident light notably impacts the performance of PDs. To further investigate the photoresponse behavior of the heterojunctions, we evaluated the photocurrent response of H2 at various light power densities. As illustrated in Supplementary Figure 4A and B, the P_{ph} increases with power density under both 0.6 and 0 V bias for all tested wavelengths of illumination. Supplementary Figure 4C and D depict the relationship between P_{ph} and optical power density (P_λ) for different wavelengths, revealing that P_{ph} rises with increasing P_λ across all wavelengths. This suggests that the heterostructure-based self-powered PD can accurately detect light of varying intensities from ultraviolet to near-infrared wavelengths in practical applications.

In contrast to the relationship between P_{ph} and P_λ, the R_{ph} decreases as P_λ increases, as demonstrated in Supplementary Figure 4E and F. This decline is attributed primarily to saturation of defect states on the heterojunction's surface at higher P_λ, which increases the recombination probability of electron-hole pairs[74]. Consequently, higher R_{ph} is achieved at lower P_λ. The P_{ph} and R_{ph} of H2-PD at 520 nm are markedly higher than at other wavelengths, reflecting the enhanced light absorption of the H2 heterojunction in this specific band. Under 520 nm illumination at a power density of 42.4 mW cm^{-2} (Level I), the maximum R_{ph} of H2-PD was 2.9 and 28.6 μA W^{-1} at 0 and 0.6 V, respectively, demonstrating excellent sensitivity to green light. Additionally, H2-PD exhibited good self-powered cycling stability over 3,000 s [Supplementary Figure 5]. Interestingly, the photocurrent did not decay monotonically: it slightly increased during the initial cycles, followed by a gradual decline upon prolonged operation. This behavior arises from the competition between initial trap-state passivation (e.g., oxygen vacancies at the heterojunction interface) that temporarily enhances charge separation, and subsequent surface degradation caused by electrolyte ion adsorption and mild structural reorganization, which together limit long-term stability to 75% retention after 3,000 s.

To further examine the transport characteristics of photogenerated carriers in the GeNSs/SiNSs heterojunction, we measured the energy level structures of GeNSs and SiNSs. Figure 5A and B show the flat band (E_{fb}) potentials *vs.* SCE (*vs.* E_{SCE}) of GeNSs and SiNSs as -1.11 and -1.0 V, respectively, obtained through Mott-Schottky measurements with a SCE as a reference. The E_{fb} values *vs.* the normal hydrogen electrode (NHE) (*vs.* E_{NHE}) were calculated to be -0.87 and -0.76 V, respectively, using $E_{NHE} = E_{SCE} + 0.2412$. Typically, the flat band potential (*vs.* E_{NHE}) is approximately 0.1 V more positive than the conduction band minimum (CBM) for an n-type semiconductor[75]. Accordingly, the conduction band edge positions (E_{CB}) of GeNSs and SiNSs were -0.97 and -0.86 V, respectively. By combining these with the band gap values, the full energy band positions of GeNSs and SiNSs were obtained, as shown in Figure 5C. This indicates that when GeNSs and SiNSs are in contact, either a direct Z-scheme heterojunction or a type-II heterojunction may form, effectively promoting the separation of photogenerated electrons and holes, thereby enhancing the photocurrent response and providing insight into the mechanism by which the GeNSs/SiNSs heterojunction improves PD performance[76,77].

Tartrazine, an azo-type acidic dye commonly used as a food additive, can pose health risks when consumed in excess. To evaluate the analytical performance of the GeNSs/SiNSs-based PEC sensor, we measured the photocurrents of the H2 electrode in various tartrazine concentrations with 0.1 M Na_2SO_4 as the supporting electrolyte (see the Section "EXPERIMENTAL" for detailed experimental procedures). Pulsed light

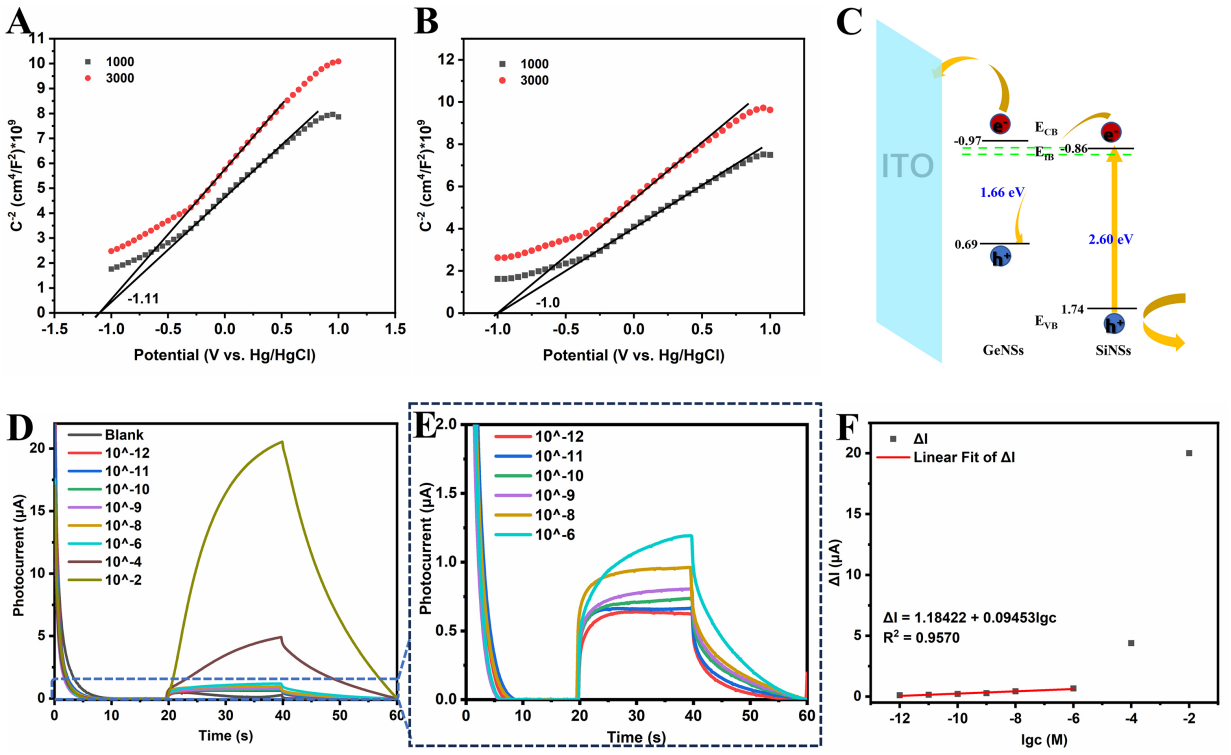

Figure 5. (A) Mott-Schottky curve of GeNSs; (B) Mott-Schottky curve of SiNSs; (C) Energy level structures of GeNSs and SiNSs. (D) Photocurrent responses of the electrode with different concentrations of tartrazine under 520 nm illumination (Level III) and a bias potential of 0.3 V. (E) Photocurrent responses of the electrode with tartrazine concentrations of 10^{-12}, 10^{-11}, 10^{-10}, 10^{-9}, 10^{-8}, and 10^{-6} M. (F) A scatter plot and fitted line of photocurrent *vs.* log of tartrazine concentration.

irradiation was applied with a fixed period of 20 s light on followed by 20 s off; the light power density was kept constant at Level III as defined in Supplementary Table 1. As shown in Figure 5D and E, under 520 nm illumination (Level III) and a bias potential of 0.3 V, the photocurrent of H2 increased with higher tartrazine concentrations. This enhancement results from the direct oxidation of tartrazine by photogenerated holes in the valence band of SiNSs, which reduces recombination of electron-hole pairs, and allows greater accumulation of free electrons in the conduction band of GeNSs. The increase in photocurrent can then be measured as a function of tartrazine concentration. A strong linear relationship was observed between the logarithm of tartrazine concentration (10^{-12}-10^{-6} M) and the photocurrent change (ΔI), described by the linear fitting equation: $\Delta I = 1.18422 + 0.09453\lg c$ ($R^2 = 0.957$) [Figure 5F]. The linear detection range spanned from 1 pM to 1 μM, with a limit of detection (LOD) estimated at 2.97×10^{-13} M (~0.3 pM). Beyond this range, at tartrazine concentrations ≥ 10^{-4} M, the photocurrent increase deviates from linearity due to surface saturation and Langmuir-type adsorption behavior, where the active sites on the electrode become fully occupied, altering the charge-transfer mechanism and interfacial electric field. As summarized in Supplementary Table 3, compared with other reported tartrazine sensors (including electrochemical, fluorescence, and PEC sensors), our PEC sensor achieves a remarkably lower LOD (0.3 pM) than most existing sensors, benefiting from the efficient Z-scheme charge separation and the strong photoresponse at 520 nm, which matches the absorption band of tartrazine. Additionally, the sensor exhibited excellent stability over ten on-off irradiation cycles [Supplementary Figure 6], highlighting its promise for practical applications in environmental and food safety monitoring.

The electron transfer mechanism of the GeNSs/SiNSs heterojunction was further analyzed using techniques including electron paramagnetic resonance (EPR) and *in situ* XPS. EPR results [Figure 6A and B] show that under illumination, both $\bullet O_2^-$ and •OH radicals exhibit evident signals in the H2 heterojunction, ruling out

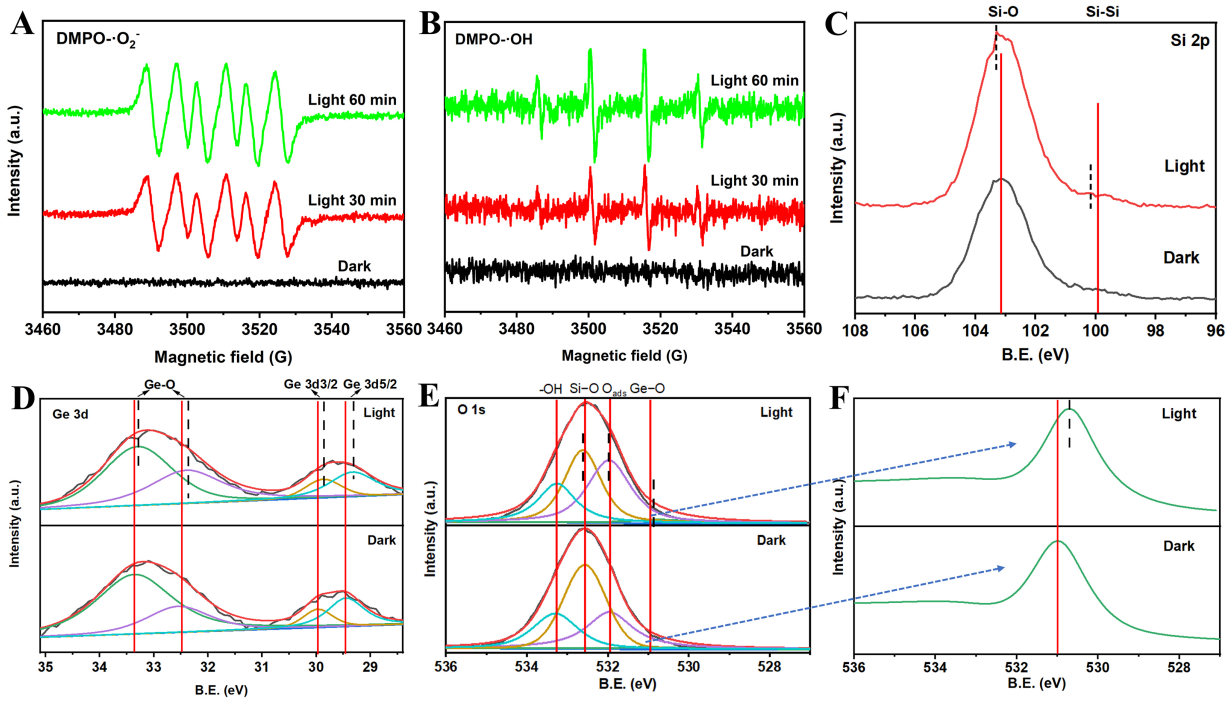

Figure 6. (A) EPR results for $\bullet O_2^-$ of H2 heterojunction under dark and Xe lamp light (30 and 60 min); (B) EPR results for •OH of H2 heterojunction under dark and light (30 and 60 min). (C-F) The *in situ* high-resolution XPS spectra for H2 heterojunction under dark and Xe lamp light: (C) Si 2p, (D) Ge 3d, (E) O 1s. (F) Partial enlarged view of (E).

the type-II mechanism (under which the valence band position is insufficient to generate •OH). The Z-scheme mechanism is more consistent with the radical generation characteristics of this system: after photogenerated electrons and holes recombine at the heterointerface, they retain highly reductive electrons and highly oxidative holes, respectively, effectively driving O_2 reduction and H_2O oxidation processes. The peak-fitted *in situ* XPS spectra [Figure 6C-F] show that under illumination, the Si 2p binding energy increases while the Ge 3d binding energy decreases, indicating that photogenerated electrons flow from Si to Ge, consistent with the Z-scheme charge transfer pathway. The shift behavior of the O 1s peak is fully coordinated with the changes in the Ge 3d and Si 2p peaks. The characteristic peak of Ge-O (530.8 eV) shifts toward lower binding energy after illumination, while the characteristic peak of Si-O (532.6 eV) shifts positively, in complete agreement with the changes in electron density of GeNSs and SiNSs. The interfacial adsorbed oxygen (O_{ads}) peak at 531.95 eV, originating from oxygen vacancies, shows only a minor change in intensity after illumination, further ruling out surface oxidation interference induced by light and demonstrating that the shifts in orbital binding energies are dominated by photogenerated carrier recombination rather than surface chemical oxidation.

Combining the above EPR and *in situ* XPS evidence, the PEC sensing mechanism of the GeNSs/SiNSs heterojunction for tartrazine detection is schematically illustrated in Figure 7A and can be described as follows. In this Z-scheme heterojunction system, upon light irradiation, the photogenerated electrons in the conduction band of SiNSs recombine with the photogenerated holes in the valence band of GeNSs through the heterointerface, leaving highly reductive electrons in the conduction band of GeNSs and highly oxidative holes in the valence band of SiNSs. The EPR results confirm the coexistence of $\bullet O_2^-$ and •OH radicals, which is characteristic of the Z-scheme mechanism rather than the type-II mechanism. When the target molecule tartrazine (an electron donor) is present in solution, it is preferentially oxidized by the strongly oxidizing holes accumulated in the valence band of SiNSs. This process effectively suppresses the recombination of photogenerated carriers, leading to an increased electron density in the conduction band of GeNSs, which

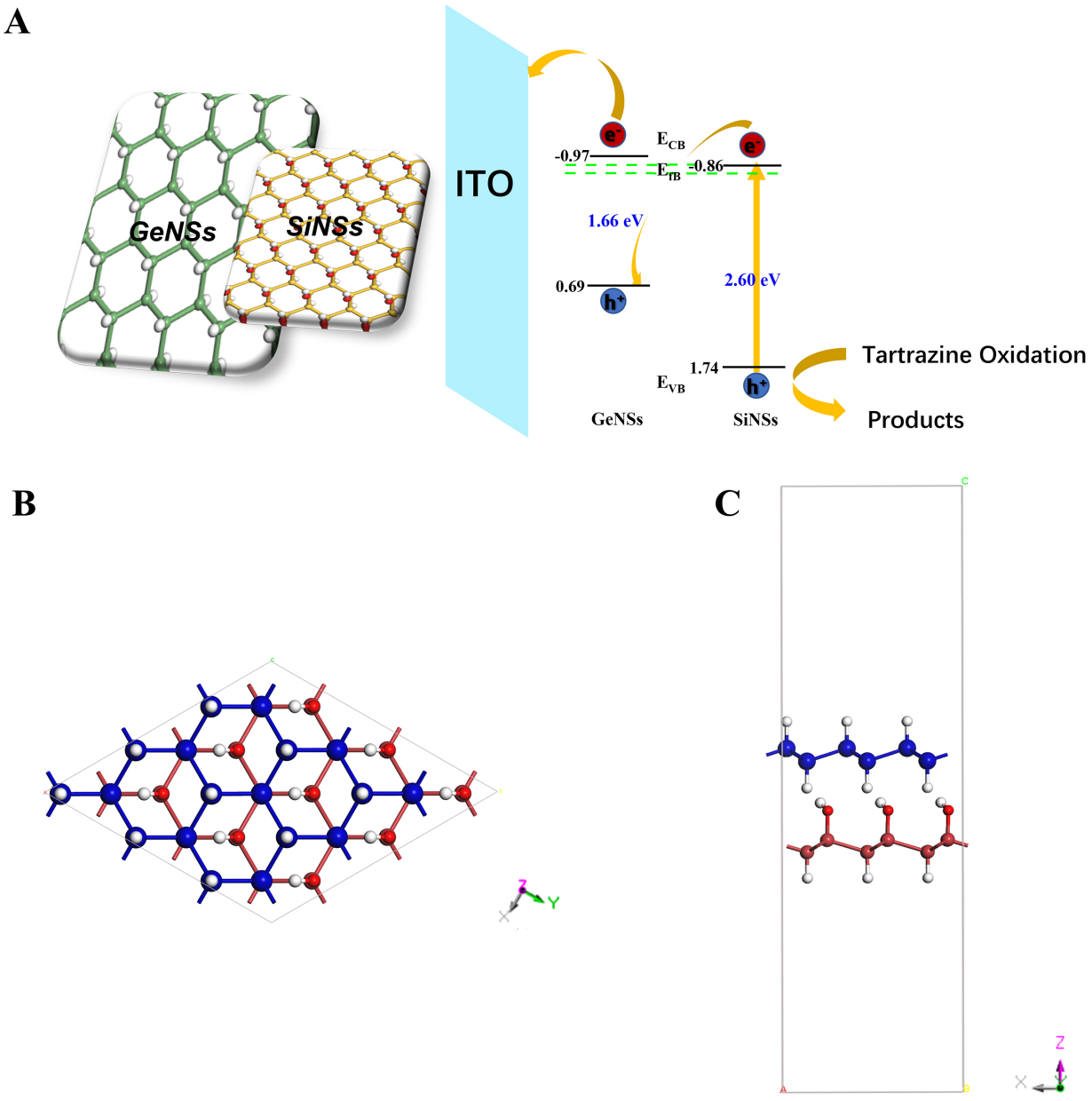

Figure 7. (A) Schematic diagram of the energy level structure of GeNSs/SiNSs Z-scheme heterojunction and the mechanism of detecting tartrazine. (B and C) The structure of germanane/siloxene heterostructure with clearly labeled x-, y-, and z-axes: (B) Top view, (C) Side view.

macroscopically manifests as a marked increase in photocurrent. The photocurrent increment (ΔI) exhibits a good linear relationship with the tartrazine concentration in the range of 1 pM to 1 μM, enabling highly sensitive detection of tartrazine.

THEORETICAL ANALYSIS

To gain a deeper understanding of the electron transfer mechanisms in GeNSs/SiNSs heterojunctions, we simulated a van der Waals (vdW) heterostructure by constructing a thermodynamically favorable structure of a germanane/siloxene heterobilayer, where the germanane and siloxene frameworks are stacked in an AB stacking[78,79], as shown in Figure 7B and C. To determine the most stable stacking structure of the heterobilayer, we systematically calculated the binding energy of the heterostructure with interlayer distances

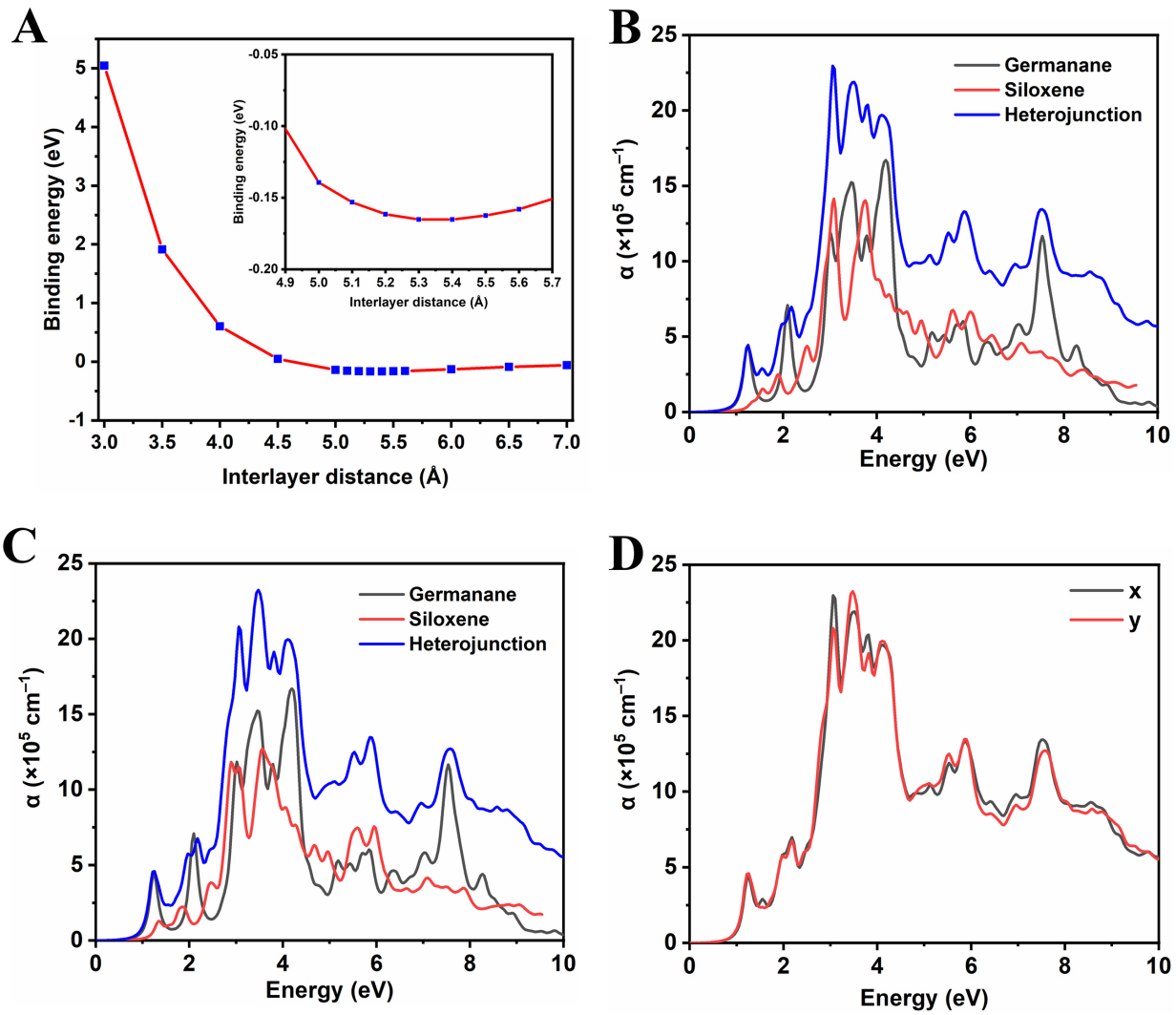

Figure 8. The optical properties of the germanane/siloxene heterostructure. (A) Calculated energy curve of germanane/siloxene as a function of interlayer distance. (B and C) represent the optical absorption coefficient α of the isolated germanane and siloxene layers and the germanane/siloxene heterostructure in the *x* and *y* directions, respectively. (D) Comparison of the optical absorption coefficient α of germanane/siloxene in the *x* and *y* directions.

ranging from 3.0 to 7.0 Å. The calculation results confirm that the heterobilayer achieves the lowest binding energy and optimal thermodynamic stability at an interlayer distance of 5.3 Å [Figure 8A]. This heterostructure is a direct bandgap semiconductor, similar to the germanane and siloxene monolayers, but has a smaller bandgap (1.898 eV) than those of the individual monolayers [Supplementary Figure 7A-C], suggesting that electron excitation from the valence band maximum (VBM) to the CBM in the heterostructure occurs more easily under visible light irradiation compared to the monolayers. The total density of states reveals that the CBM of the heterojunction is primarily composed of states from the germanane layer, while the VBM is contributed by states from the siloxene layer [Supplementary Figure 7D]. Therefore, the electrons and holes in the germanane/siloxene heterojunction are distributed in the germanane and siloxene layers, respectively, which facilitates the separation of electrons and holes.

The calculations of optical properties indicate slight differences in the light absorption coefficients of the siloxene monolayer and the heterostructure in the x and y directions [Figure 8B and C]. However, the light absorption coefficient curves for the bilayer heterojunction in the x and y directions nearly overlap [Figure 8D], indicating that the light absorption capacity of the bilayer heterojunction is nearly consistent

across different directions. In comparison to the monolayers of germanane and siloxene, the light absorption range of the heterojunction encompasses the combined absorption ranges of both, with a pronouncedly enhanced light absorption intensity, especially in the ultraviolet region. This computational result theoretically explains the mechanism behind the marked improvement in the photoelectric performance of the GeNSs/SiNSs heterojunction, demonstrating that the enhanced light absorption of the heterostructure is more suitable for optoelectronic devices.

CONCLUSIONS

In conclusion, we successfully constructed direct Z-scheme 2D-2D GeNSs/SiNSs heterojunctions for the first time, which demonstrate potential for self-powered, broadband-response, and high-sensitivity PEC PDs. The formation of these direct Z-scheme heterojunctions substantially enhances the separation of photogenerated electrons and holes, thereby improving the redox capability of the composite materials and consequently boosting the photocurrent response. Furthermore, the heterojunctions effectively extend the light absorption range of SiNSs, enabling a broader spectrum of light detection. The optimal mass ratio of GeNSs to SiNSs was determined to be 3:7, which yielded superior performance compared with pure GeNSs and SiNSs. Notably, the PEC PD based on the GeNSs/SiNSs heterojunction exhibited the strongest light response at 520 nm and also demonstrated its capability as a PEC sensor for detecting the common azo food additive tartrazine. This sensor showcased a wide linear detection range for tartrazine concentration along with an ultra-low detection limit, underscoring the considerable application potential of GeNSs/SiNSs heterojunctions in high-sensitivity and low-detection-limit PEC sensors. Although the present data were collected from three representative mass ratios, we acknowledge that a more detailed compositional series would be necessary to pinpoint the exact optimum. Future work could combine systematic TEM-EDS mapping and local photocurrent measurements to directly correlate the spatial distribution of GeNSs and SiNSs with the photoresponse at the nanoscale, thereby providing direct experimental verification of the optimal distribution and the role of heterointerface density.

DECLARATIONS

Acknowledgments

The authors would like to thank Shiyanjia Lab (www.shiyanjia.com) for the Raman spectroscopy, XPS and EPR measurements, and thank Ceshigo for the DFT calculations. In addition, the authors would like to thank Bo Song from SCI-GO (www.sci-go.com) for the SEM and *in situ* XPS measurements.

Authors' contributions

Conception and design of the work: Zhao, F.
Data acquisition and analysis: Liu, R.; Chen, H.
Writing - original draft, data interpretation: Zhao, F.; Liu, R.; Chen, H.
Investigation: Yuan, W.; Fu, H.
Writing - review and editing: Zhao, F.; Feng, Y.

Availability of data and materials

The data supporting the findings of this study are available within this Article and its Supplementary Materials. Further data are available from the corresponding authors upon request.

AI and AI-assisted tools statement

Not applicable.

Financial support and sponsorship

This work was supported by the Taishan Scholar Project of Shandong Province of China (Grant No. tsqn202312187), the Natural Science Foundation of Shandong Province (ZR2024QE220), and the National Natural Science Foundation of China (Grant No. 52103093).

Conflicts of interest

Zhao, F. is affiliated with Shandong Chambroad Holding Group Co., Ltd., The other authors declared that there are no conflicts of interest.

Ethical approval and consent to participate

Not applicable.

Consent for publication

Not applicable.

Supplementary Materials

Supplementary Materials

REFERENCES

1. Li, X.; Wang, S.; Bi, Y.; Shen, Z.; Han, J.; Li, H. Recent advances in 2D nanomaterials as photocatalysts for sustainable CO_2 reduction. *Chem. Eng. J.* **2026**, *542*, 178146. DOI
2. Tang, J.; Guo, C.; Wang, T.; et al. A review of g-C_3N_4-based photocatalytic materials for photocatalytic CO_2 reduction. *Carbon. Neutral.* **2024**, *3*, 557-83. DOI
3. Yang, Z.; Ji, Y.; Ren, J.; Wang, X.; Xue, Y.; Tian, J. 2D/2D heterointerface engineering of $Ni_2P/ZnIn_2S_4$ photocatalysts for enhanced photocatalytic H_2 evolution. *Mater. Rep. Energy.* **2026**, *6*, 100401. DOI
4. Wu, R.; He, C.; Meng, X.; et al. Competition between phonon-assisted and exciton photoluminescence modulated by temperature in WSe_2/graphene nanosheet heterostructures for flexible optoelectronic sensor devices. *ACS. Appl. Nano. Mater.* **2024**, *7*, 16941-8. DOI
5. Chen, J.; Bailey, C. S.; Cui, D.; et al. Stacking independence and resonant interlayer excitation of monolayer $WSe_2/MoSe_2$ heterostructures for photocatalytic energy conversion. *ACS. Appl. Nano. Mater.* **2020**, *3*, 1175-81. DOI
6. Zhao, F.; Feng, Y.; Feng, W. Germanium-based monoelemental and binary two-dimensional materials: theoretical and experimental investigations and promising applications. *InfoMat* **2022**, *4*, e12365. DOI
7. Nakano, H.; Ishii, M.; Nakamura, H. Preparation and structure of novel siloxene nanosheets. *Chem. Commun.* **2005**, *23*, 2945-7. DOI PubMed
8. Bianco, E.; Butler, S.; Jiang, S.; Restrepo, O. D.; Windl, W.; Goldberger, J. E. Stability and exfoliation of germanane: a germanium graphane analogue. *ACS. Nano.* **2013**, *7*, 4414-21. DOI PubMed
9. Jiang, S.; Arguilla, M. Q.; Cultrara, N. D.; Goldberger, J. E. Covalently-controlled properties by design in group IV graphane analogues. *Acc. Chem. Res.* **2014**, *48*, 144-51. DOI
10. Xiao, M.; Yin, X.; Song, H.; Lv, Y.; Xiao, B. Tunable band gaps and high carrier mobilities in germanene by Si doping in the presence of an external electric field: field effect transistors. *Phys. B. Condens. Matter.* **2024**, *682*, 415859. DOI
11. Madhushankar, B. N.; Kaverzin, A.; Giousis, T.; et al. Electronic properties of germanane field-effect transistors. *2D. Mater.* **2017**, *4*, 021009. DOI
12. Liu, N.; Qiao, H.; Xu, K.; et al. Hydrogen terminated germanene for a robust self-powered flexible photoelectrochemical photodetector. *Small* **2020**, *16*, 2000283. DOI
13. Roy, P. K.; Hartman, T.; Šturala, J.; Luxa, J.; Melle-Franco, M.; Sofer, Z. Hydrogen-terminated two-dimensional germanane/silicane alloys as self-powered photodetectors and sensors. *ACS. Appl. Mater. Interfaces.* **2023**, *15*, 25693-703. DOI PubMed PMC
14. Zhang, Q.; Ziad, M.; Liu, Z.; Li, H.; Fu, A. Germanene/MoS_2 heterostructure as promising anchoring and electrocatalyzing material for high performance lithium-sulfur batteries: a computational study. *J. Energy. Storage.* **2025**, *109*, 115205. DOI
15. Wu, B.; Šturala, J.; Veselý, M.; et al. Functionalized germanane/SWCNT hybrid films as flexible anodes for lithium-ion batteries. *Nanoscale. Adv.* **2021**, *3*, 4440-6. DOI
16. Zhang, X.; Xin, L.; Murugesan, K.; et al. Two-dimensional siloxene: a promising silicon-based material with enhanced volume stability for Li-ion battery anode. *Chem. Eng. J.* **2026**, *532*, 174513. DOI
17. Guo, Q.; Han, Y.; Chen, N.; Qu, L. Few-layer siloxene as an electrode for superior high-rate zinc ion hybrid capacitors. *ACS. Energy. Lett.* **2021**, *6*, 1786-94. DOI
18. Zhang, E.; Xie, D.; Hong, Y.; et al. Siloxene coupled graphene anode membrane with Zn-ion intercalation for all-solid-state Zn-ion hybrid supercapacitors. *Chem. Eng. J.* **2025**, *523*, 168578. DOI

19. Huang, Y.; Xiao, S.; Zhong, Z.; et al. A novel ratiometric biosensor based on germanene nanosheets for rapid and sensitive BRCA1 detection in differentiating T cells. *Biosens. Bioelectron.* **2026**, *298*, 118411. DOI
20. Song, Z.; Ang, W. L.; Sturala, J.; et al. Functionalized germanene-based nanomaterials for the detection of single nucleotide polymorphism. *ACS. Appl. Nano. Mater.* **2021**, *4*, 5164-75. DOI
21. Kovalska, E.; Antonatos, N.; Luxa, J.; Sofer, Z. Edge-hydrogenated germanene by electrochemical decalcification-exfoliation of $CaGe_2$: germanene-enabled vapor sensor. *ACS. Nano.* **2021**, *15*, 16709-18. DOI PubMed
22. Ramachandran, R.; Leng, X.; Zhao, C.; Xu, Z.; Wang, F. 2D siloxene sheets: a novel electrochemical sensor for selective dopamine detection. *Appl. Mater. Today.* **2020**, *18*, 100477. DOI
23. Rosli, N. F.; Rohaizad, N.; Sturala, J.; Fisher, A. C.; Webster, R. D.; Pumera, M. Siloxene, germanane, and methylgermanane: functionalized 2D materials of group 14 for electrochemical applications. *Adv. Funct. Mater.* **2020**, *30*, 1910186. DOI
24. Giousis, T.; Fang, S.; Miola, M.; et al. Germanane and butyl-functionalized germanane as visible-light photocatalysts for the degradation of water pollutants. *J. Environ. Chem. Eng.* **2023**, *11*, 109784. DOI
25. Li, S.; Wang, H.; Li, D.; et al. Siloxene nanosheets: a metal-free semiconductor for water splitting. *J. Mater. Chem. A.* **2016**, *4*, 15841-4. DOI
26. Ng, S.; Sturala, J.; Vyskocil, J.; et al. Two-dimensional functionalized germananes as photoelectrocatalysts. *ACS. Nano.* **2021**, *15*, 11681-93. DOI
27. Zhao, F.; Feng, Y.; Wang, Y.; et al. Two-dimensional gersiloxenes with tunable bandgap for photocatalytic H_2 evolution and CO_2 photoreduction to CO. *Nat. Commun.* **2020**, *11*, 1443. DOI PubMed PMC
28. Li, M.; Ramachandran, R.; Sakthivel, T.; Wang, F.; Xu, Z. Siloxene: an advanced metal-free catalyst for efficient photocatalytic reduction of aqueous Cr(VI) under visible light. *Chem. Eng. J.* **2021**, *421*, 129728. DOI
29. Imagawa, H.; Wu, X.; Itahara, H.; et al. Photocatalytic NO removal over calcium-bridged siloxenes under ultraviolet and visible light irradiation. *Dalton. Trans.* **2018**, *47*, 7070-6. DOI
30. Luo, J.; Selopal, G. S.; Tong, X.; Wang, Z. Colloidal quantum dots and two-dimensional material heterostructures for photodetector applications. *Electron* **2024**, *2*, e30. DOI
31. Xiao, J.; Xiong, X.; Shi, X.; et al. High-performance edge-contact monolayer molybdenum disulfide transistors. *Research* **2025**, *8*, 0593. DOI PubMed PMC
32. Qiu, D.; Gong, C.; Wang, S.; et al. Recent advances in 2D superconductors. *Adv. Mater.* **2021**, *33*, 2006124. DOI
33. Wang, Y.; Zhao, F.; Wang, Y.; et al. Broadband self-powered photoelectrochemical photodetector based on Te/Se heterostructure nanocomposites. *Compos. Commun.* **2022**, *32*, 101175. DOI
34. Li, P.; Deng, D.; Liu, Y.; et al. Unveiling the defect-accelerated charge transfer mechanism in $ZnIn_2S_4$/g-C_3N_4 Z-scheme heterojunctions for efficient solar fuel production. *Carbon. Neutral.* **2026**, *5*, e70139. DOI
35. Tan, X.; Loh, J. Y.; Mohamed, A. R.; Ong, W. Two-in-one redox photocatalysis: cooperative hydrogen evolution and benzaldehyde production via 2D MoS_2 cocatalyst-loaded hydrangea-like $Zn_3In_2S_6$. *Mater. Rep. Energy.* **2025**, *5*, 100374. DOI
36. Lee, J.; Kim, Y.; Kwak, B. S.; et al. Atomic-scale structurally locked 1T/2H-MoS_2/ZnS Z-scheme heterojunctions for prolonged charge kinetics and dual-functional photocatalysis. *Energy. Environ. Mater.* **2026**, e70493. DOI
37. Yu, H.; Wu, X. Ripples in two-dimensional transition metal sulfides: formation mechanism, optoelectronic regulation, and application prospects. *Battery. Energy.* **2026**, *5*, e70108. DOI
38. Ding, G.; Wang, Z.; Zhang, J.; Wang, P.; Chen, L.; Liao, G. Layered double hydroxides-based Z-scheme heterojunction for photocatalysis. *EcoEnergy* **2024**, *2*, 22-44. DOI
39. Yuan, M.; Jiang, L.; Mao, S.; Zhou, W.; Lin, X.; Yuan, Y. Construction Z-scheme heterostructure by WO_3 nanocubes embedded g-C_3N_4 nanosheets with n-π* electronic transition for enhanced visible light driven photocatalysis. *J. Photochem. Photobiol. A. Chem.* **2025**, *469*, 116581. DOI
40. Zhu, Q.; Sun, J.; Zhu, Y.; Jiang, H.; Yan, W.; Shen, J. In situ phase transition and Cu doping synergistically regulate perovskite Z-scheme heterojunction for photocatalytic CO_2 reduction. *Energy. Environ. Mater.* **2026**, e70387. DOI
41. Mandari, K. K.; Kang, M. g-C_3N_4/MXene-based heterostructures: advanced catalysts for efficient and sustainable renewable energy production. *Adv. Ind. Eng. Chem.* **2025**, *1*, 14. DOI
42. Wang, S.; Hao, W.; Liu, Z.; Niu, X.; Wang, L.; Zhao, Q. Two-dimensional direct *Z*-scheme heterojunction photocatalysts for highly efficient energy conversion and chemical synthesis. *ACS. Nano.* **2025**, *20*, 137-62. DOI
43. Li, Y.; Wang, J. 2D/2D*Z*-scheme WO_3/g-C_3N_4 heterojunctions for photocatalytic organic pollutant degradation and nitrogen fixation. *Mater. Adv.* **2024**, *5*, 749-61. DOI

44. Tuc Altaf, C.; Yaman, E.; Karagoz, E.; Colak, Colak.; Demirci Sankir, E.; Sankir, M. Self-powered photoelectrochemical photodetectors based on a $CsPbBr_3$/S-g-C_3N_4 heterojunction-sensitized 3D ZnO nanostructured thin film. *ACS. Appl. Nano. Mater.* **2024**, *7*, 8186-96. DOI
45. Xiao, W.; Xu, W.; Huang, W.; et al. Bismuth-based BiO Br_xI_{1-x}/Ti_3C_2 MXene schottky nanocomposites for Hg^{2+} photoelectrochemical sensors. *ACS. Appl. Nano. Mater.* **2022**, *5*, 18168-77. DOI
46. Qu, J.; Cheng, H.; Lan, H.; et al. Space-confined growth of ultrathin P-type GeTe nanosheets for broadband photodetectors. *Small* **2024**, *20*, 2309391. DOI
47. Yang, W.; Chen, T.; Xie, L.; Yu, Y.; Long, M.; Xu, L. A systematic study of switching, optoelectronics, and gas-sensitive properties of PCF-graphene-based nanodevices: insights from DFT study. *Carbon. Neutral.* **2024**, *3*, 904-17. DOI
48. Zeng, W.; Zhang, Y.; Wu, Z.; et al. Hierarchically converged defect engineering with 2-dimensional black phosphorus/MXene sequence for sensitive photoelectrochemical-electrostatic sensors. *Research* **2025**, *8*, 0966. DOI PubMed PMC
49. Qin, J.; Tang, Y.; Zeng, Y.; Liu, X.; Tang, D. Recent advances in flexible sensors: from sensing materials to detection modes. *TrAC. Trends. Anal. Chem.* **2024**, *181*, 118027. DOI
50. Awasthi, T.; Kaur, S.; Joshi, S.; Kaur, R. Advances in smart indicators and their integration with sensor systems for foodborne hazard monitoring. *Food. Control.* **2026**, *183*, 111932. DOI
51. Bhardwaj, S. K.; Deep, A.; Bhardwaj, N.; Wangoo, N. Recent advancements in nanomaterial based optical detection of food additives: a review. *Analyst* **2023**, *148*, 5322-39. DOI PubMed
52. Han, J.; Fu, Z.; Wei, J.; et al. 2D materials-based next-generation multidimensional photodetectors. *Light. Sci. Appl.* **2025**, *14*, 362. DOI PubMed PMC
53. Qiu, Z.; Tang, D. Nanostructure-based photoelectrochemical sensing platforms for biomedical applications. *J. Mater. Chem. B.* **2020**, *8*, 2541-61. DOI PubMed
54. Ali, M. A.; Tchalala, M. R. Chemical synthesis of silicon nanosheets from layered calcium disilicide. *J. Phys. Conf. Ser.* **2014**, *491*, 012009. DOI
55. Hui, X.; Li, L.; Xia, Q.; et al. Interface engineered Sb_2O_3/$W_{18}O_{49}$ heterostructure for enhanced visible-light-driven photocatalytic N_2 reduction. *Chem. Eng. J.* **2022**, *438*, 135485. DOI
56. Jiang, H.; Zhu, X.; Wang, D.; et al. Tunable type-I band alignment and electronic structure of GaSe/$MoSi_2N_4$ van der Waals heterostructure. *Microstructures* **2025**, *5*, 2025009. DOI
57. Sturala, J.; Luxa, J.; Matějková, S.; et al. Exfoliation of Calcium germanide by alkyl halides. *Chem. Mater.* **2019**, *31*, 10126-34. DOI
58. Liu, N.; Xu, K.; Lei, Y.; et al. Germanene nanosheets: achieving superior sodium-ion storage via pseudointercalation reactions. *Small. Struct.* **2021**, *2*, 2100041. DOI
59. Chang, C.; Yang, H.; Mu, W.; et al. In situ fabrication of bismuth oxyiodide ($Bi_7O_9I_3$/Bi_5O_7I) n-n heterojunction for enhanced degradation of triclosan (TCS) under simulated solar light irradiation. *Appl. Catal. B. Environ.* **2019**, *254*, 647-58. DOI
60. Hu, K.; Tian, J.; Zhou, Z.; Zhao, D.; Guan, X. Direct Z-scheme photocatalytic systems based on vdW heterostructures for water splitting and CO_2 reduction: fundamentals and recent advances. *Microstructures* **2024**, *4*, 2024021. DOI
61. Kong, X. Y.; Choo, Y. Y.; Chai, S.; Soh, A. K.; Mohamed, A. R. Oxygen vacancy induced Bi_2WO_6 for the realization of photocatalytic CO_2 reduction over the full solar spectrum: from the UV to the NIR region. *Chem. Commun.* **2016**, *52*, 14242-5. DOI
62. Lu, Y.; Chen, M.; Huang, T.; et al. Oxygen vacancy-dependent photocatalytic activity of well-defined $Bi_2Sn_2O_{7-x}$ hollow nanocubes for NO_x removal. *Environ. Sci. Nano.* **2021**, *8*, 1927-33. DOI
63. Ni, H.; Li, M.; Hu, Y.; et al. Two-dimensional SnSe/GeSe van der Waals heterostructure with strain-tunable electronic and optical properties. *J. Phys. Chem. Solids.* **2019**, *131*, 223-9. DOI
64. Ma, J.; Xu, L.; Yin, Z.; et al. "One stone four birds" design atom co-sharing BiOBr/Bi_2S_3 S-scheme heterojunction photothermal synergistic enhanced full-spectrum photocatalytic activity. *Appl. Catal. B. Environ. Energy.* **2024**, *344*, 123601. DOI
65. Cultrara, N. D.; Wang, Y.; Arguilla, M. Q.; et al. Synthesis of 1T, 2H, and 6R germanane polytypes. *Chem. Mater.* **2018**, *30*, 1335-43. DOI
66. Ren, X.; Li, Z.; Huang, Z.; et al. Environmentally robust black phosphorus nanosheets in solution: application for self-powered photodetector. *Adv. Funct. Mater.* **2017**, *27*, 1606834. DOI
67. Wang, B.; Zhu, W.; Tang, P.; Qi, X. Graphene-like tungsten sulphide nanosheets prepared by hydrothermal intercalation/exfoliation route and its application for photodetector. *Fullerenes. Nanotubes. Carbon. Nanostruct.* **2019**, *27*, 928-33. DOI
68. Xie, Z.; Xing, C.; Huang, W.; et al. Ultrathin 2D nonlayered tellurium nanosheets: facile liquid-phase exfoliation, characterization, and photoresponse with high performance and enhanced stability. *Adv. Funct. Mater.* **2018**, *28*, 1705833. DOI

69. Huang, H.; Ren, X.; Li, Z.; et al. Two-dimensional bismuth nanosheets as prospective photo-detector with tunable optoelectronic performance. *Nanotechnology* **2018**, *29*, 235201. DOI
70. Fan, T.; Xie, Z.; Huang, W.; Li, Z.; Zhang, H. Two-dimensional non-layered selenium nanoflakes: facile fabrications and applications for self-powered photo-detector. *Nanotechnology* **2019**, *30*, 114002. DOI
71. Li, Z.; Qiao, H.; Guo, Z.; et al. High-performance photo-electrochemical photodetector based on liquid-exfoliated few-layered InSe nanosheets with enhanced stability. *Adv. Funct. Mater.* **2017**, *28*, 1705237. DOI
72. Qiao, H.; Chen, X.; Wang, B.; Huang, Z.; Qi, X. Novel tin disulfide/graphene photoelectrochemical photodetector based on solid-state electrolytes and its performances. *J. Mater. Sci. Mater. Electron.* **2019**, *30*, 3208-13. DOI
73. Ren, X.; Qiao, H.; Huang, Z.; et al. Investigating the photocurrent generation and optoelectronic responsivity of WS_2-TiO_2 heterostructure. *Opt. Commun.* **2018**, *406*, 118-23. DOI
74. Lan, C.; Li, C.; Yin, Y.; Guo, H.; Wang, S. Synthesis of single-crystalline GeS nanoribbons for high sensitivity visible-light photodetectors. *J. Mater. Chem. C.* **2015**, *3*, 8074-9. DOI
75. Li, Y.; Sun, B.; Lin, H.; et al. Efficient visible-light induced H_2 evolution from T-$Cd_xZn_{1-x}S$/defective MoS_2 nano-hybrid with both bulk twinning homojunctions and interfacial heterostructures. *Appl. Catal. B. Environ.* **2020**, *267*, 118702. DOI
76. Li, X.; Wan, Y.; Deng, F.; et al. Advances in Z-scheme and S-scheme heterojunctions for photocatalytic and photoelectrocatalytic H_2O_2 production. *Chin. Chem. Lett.* **2025**, *36*, 111418. DOI
77. Chen, X.; Wu, W.; Zhang, Q.; et al. Z-scheme Bi_2O_3/$CuBi_2O_4$ heterojunction enabled sensitive photoelectrochemical detection of aflatoxin B1 for health care, the environment, and food. *Biosens. Bioelectron.* **2022**, *214*, 114523. DOI
78. Jin, H.; Dai, Y.; Ma, X.; Yu, L.; Wei, W.; Huang, B. Enhancement of photocatalytic activity of a two-dimensional GeH/graphene heterobilayer under visible light. *RSC. Adv.* **2015**, *5*, 52264-8. DOI
79. Louafi, W.; Haverkort, M. W.; Rezouali, K.; Belabbas, I.; Lounis, S. Electronic structure and elastic response of WSe_2/MoS_2 van der Waals heterostructures: effects of stacking. *Comput. Mater. Sci.* **2026**, *264*, 114485. DOI